Sulfur isotope mass-independent fractionation in impact deposits of the 3.2 billion-year-old Mapepe Formation, Barberton Greenstone Belt, South Africa

Mark van Zuilen, Pascal Philippot, Martin Whitehouse, Aivo Lepland

Sulfur isotope mass-independent fractionation in impact deposits of the 3.2 billion-year-old Mapepe Formation, Barberton Greenstone Belt, South Africa

M.A. van Zuilen [a,*], P. Philippot [a], M.J. Whitehouse [b], A. Lepland [c,d,e]

[a] *Géobiosphère Actuelle & Primitive, Institut de Physique du Globe de Paris, Sorbonne Paris Cité, Univ Paris Diderot, UMR 7154 CNRS, F-75005 Paris, France*

[b] *Swedish Museum of Natural History, Box 50007, SE104-05 Stockholm, Sweden*

[c] *Geological Survey of Norway, Leiv Eirikssons vei 39, 7491 Trondheim, Norway*

[d] *Tallinn University of Technology, Institute of Geology, 19086 Tallinn, Estonia*

[e] *Centre for Arctic Gas Hydrate, Environment and Climate, University of Tromsø, 9037 Tromsø, Norway*

Theoretical and experimental studies have shown that atmospheric SO_2 isotopologue self-shielding effects in the 190–220 nm region of the solar spectrum are the likely cause for mass independent fractionation of sulfur isotopes (S-MIF). The main products of this photochemical reaction – SO_3 and S^0 – typically define a compositional array of ca. $\Delta^{33}S/\delta^{34}S = 0.06$–$0.14$. This is at odds with the generally observed trend in Archean sulfides, which broadly defines an array of ca. $\Delta^{33}S/\delta^{34}S = 0.9$. Various explanations have been proposed, including a diminution of $\delta^{34}S$ caused by chemical and biogenic mass-dependent fractionation of sulfur isotopes (S-MDF), mixing with photolytic products produced during felsic volcanic events, or partial blocking of the low-wavelength part of the spectrum due to the presence of reduced atmospheric gases or an organic haze. Early in Earth history large meteorite impacts would have ejected dust and gas clouds into the atmosphere that shielded solar radiation and affected global climate. It is thus likely that at certain time intervals of high meteorite flux the atmosphere was significantly perturbed, having an effect on atmospheric photochemistry and possibly leaving anomalous sulfur isotopic signatures in the rock record. Here we describe the sulfur isotopic signatures in sulfides of spherule beds S2, S3 and S4 of the Barberton Greenstone Belt, South Africa. In particular, in spherule bed S3 – and to a lesser extent S4 – a trend of ca. $\Delta^{33}S/\delta^{34}S = 0.23$ is observed that closely follows the expected trend for SO_2-photolysis in the 190–220 nm spectral range. This suggests that an impact dust cloud (deposited as spherule beds), which sampled the higher region of the atmosphere, specifically incorporated products of SO_2 photolysis in the 190–220 nm range, and blocked photochemical reactions at higher wavelengths (250–330 nm band). By implication, the generally observed Archean trend appears to be the result of mixing of different MIF-S sources arising from a variety of photochemical reactions that took place in the lower part of the atmosphere.

1. INTRODUCTION

It is generally accepted that mass-independent fractionation of sulfur isotopes (S-MIF) – defined as (1) $\Delta^{33}S = \delta^{33}S - 1000 * [(1 + \delta^{34}S/1000)^{0.515} - 1]$, with (2) $\delta^{3x}S = [(^{3x}S/^{32}S)_{sample}/(^{3x}S/^{32}S)_{CDT} - 1] * 1000$ – is caused by photochemical reactions of gaseous sulfur compounds in a reduced atmosphere (Farquhar et al., 2000). In the >2.4 Ga Archean atmosphere the photolytic disproportionation of volcanic SO_2 produced elemental sulfur (S^0) and sulfate (SO_4) aerosols with a positive ($\Delta^{33}S > 0$) and

* Corresponding author. Tel.: +33 (0)183957527.
E-mail address: vanzuilen@ipgp.fr (M.A. van Zuilen).

negative ($\Delta^{33}S < 0$) S-MIF signature, respectively. Although the actual mechanism for photolytic isotope fractionation is still debated, it is clear that sulfur S-MIF is largely caused by self-shielding of SO_2 in the spectral range 190–220 nm (Lyons, 2007, 2009; Ono et al., 2013). It was recently shown that photo-excitation of SO_2 in the spectral range 250–330 nm could also lead to S-MIF (Whitehill and Ono, 2012; Whitehill et al., 2013). Furthermore, mass-independent kinetic isotope effects in reactions such as SO photolysis or $S + S_2 = S_3$, can also contribute to the S-MIF signal (Masterson et al., 2011). Overall, once S-MIF is created it requires two or more atmospheric exit channels – such as e.g. elemental sulfur aerosols (S^0) and sulphuric acid droplets (H_2SO_4) – for preservation in the rock record (Ono et al., 2003; Lyons, 2007). Since these exit channels can vary as a function of reducing conditions (presence of e.g. CH_4, hydrocarbon haze), S-MIF variation through time can provide insight in changing atmospheric compositions throughout the Archean Eon (Zerkle et al., 2012; Kurzweil et al., 2013).

Early in Earth history the relatively high frequency of large meteorite impacts would have caused ejection of dust and gas clouds into the atmosphere that shielded solar radiation and affected global climate (Toon et al., 1997). It is thus reasonable to assume that at certain time intervals of high meteorite flux the atmosphere was significantly perturbed, possibly causing anomalous sulfur isotopic signatures that could be preserved in the rock record. The actual induced changes to the atmosphere depend on the characteristics of the impact target; carbonate deposits release large amounts of CO_2 and CO, organic-rich deposits generate soot (a particularly strong absorber of short-wave radiation), evaporites release SO_2- or SO_3-gases, and ocean impacts cause the discharge of large amounts of water vapor (Pierazzo and Artemieva, 2012). A large meteorite impact could thus have caused a short-term shift in atmospheric composition, and therefore possibly have left a characteristic sulfur-MIF signature in Archean impact-related deposits. Directly after an impact a cloud of molten rock droplets is generated, which is quenched in the atmosphere and settles as spherules. Several of such impact-related spherule beds have been recognized in Early Archean terrains (Kyte et al., 2003; Lowe et al., 2003; Glikson, 2010). Their impact-related origin is substantiated by syn-sedimentary rip-up clasts (derived from high-energy erosion caused by tsunami waves), extraterrestrial Ir and Cr-isotope anomalies (Kyte et al., 2003), and the presence of Ni-spinel (Krull-Davatzes et al., 2010). Since such spherules were formed high in the atmosphere, they could have adsorbed sulfur aerosols and therefore have recorded specific photolytic isotope anomalies.

Here we present the variation of $\delta^{34}S$ and $\Delta^{33}S$ in sulfides of spherule beds in the 3.24 Ga Mapepe Formation, Fig Tree Group, Barberton Greenstone Belt, South Africa and compare this with other sediments in the Mapepe Formation and underlying Mendon Formation (Philippot et al., 2012). Furthermore, a comparison is made with the generally observed trend of Archean sulfides (Archean Reference Array, ARA), and an assessment is provided of the temporary influence of meteorite impacts on the composition and shielding capacity of the Archean atmosphere.

2. GEOLOGY AND SAMPLE DESCRIPTION

The Onverwacht Group, including the Mendon Formation, consists primarily of komatiitic and basaltic volcanic rocks, alternating with cherty sedimentary layers (Fig. 1). The overlying Fig Tree Group, including the Mapepe Formation, primarily consists of terrigenous sedimentary rocks interbedded with felsic volcaniclastic rocks. The entire sequence has been affected by hydrothermal alteration and lower greenschist-facies metamorphism. This caused serpentinization of komatiites, and pervasive silicification and/or carbonation of all igneous and sedimentary sequences. For a description of the different spherule bed units within the Barberton Greenstone Belt (BGB) we adopt here the stratigraphy given in Lowe et al. (2003) (Fig. 1). Spherule bed S2 occurs in the southern part of the BGB at the base of the Fig Tree Group and has been dated at 3260 Ma (Byerly et al., 1996). It consists of a low proportion of spherules (predominantly <10%, and up to 50% at the type locality) mixed with silt to cobble-sized cherty detritus eroded from cherts and komatiitic volcanic units of the underlying Mendon Formation (Lowe et al., 2003). Two separate graded beds have been identified in S2 that have been interpreted as the result of surge-like current and/or wave events associated with an impact event (Lowe et al., 2003). In the southern part of the BGB, spherule bed S3 occurs within the Mapepe Formation about 50–150 m above the base of the Fig Tree Group (Fig. 1). In the northern part of the of the BGB, the Onverwacht-Fig Tree contact is dated at 3243 Ma (Kröner et al., 1991), and spherule bed S3 occurs directly at the base of the Fig Tree Group (Fig. 1). At its type locality in the southern part of the BGB, S3 occurs as a 70 cm layer within a silicified section of sandstone, mudstone and conglomerate, called Jay's Chert (Lowe and Nocita, 1999). S3 is the most widely outcropping spherule bed in the BGB, and has been studied in great detail (Krull-Davatzes et al., 2012). Several examples have been shown of S3 slabs that consist entirely of 0.1–4 mm size spherules (Lowe et al., 2003), and a variety of spherule types have been described in literature. In some sections that show little or no evidence of reworking by currents, a bimodal distribution is observed of large silica-rich spherules (microcrystalline quartz with relict fan-shaped growth textures) and smaller Cr-rich sericite spherules (Lowe and Byerly, 1986). Both types commonly have thin, opaque rutile-rich rims. Minor mineral phases in these spherule beds typically include chlorite, spinel, apatite, rutile, barite, feldspar, siderite, and sulfide minerals (primarily pyrite, and minor chalcopyrite). Diagenesis and metamorphism have caused pervasive alteration of all mineral phases, the only intact primary mineral phase being Ni-rich chromite (Krull-Davatzes et al., 2012). Spherule bed S4 is only known from one outcrop, stratigraphically 6 meters above S3, within Jay's Chert. It consists largely of spherules, irregular chlorite-rich grains, and fine chloritic matrix, and occurs interbedded with coarse, conglomeratic, highly energetic fan-delta deposits (Lowe et al., 2003).

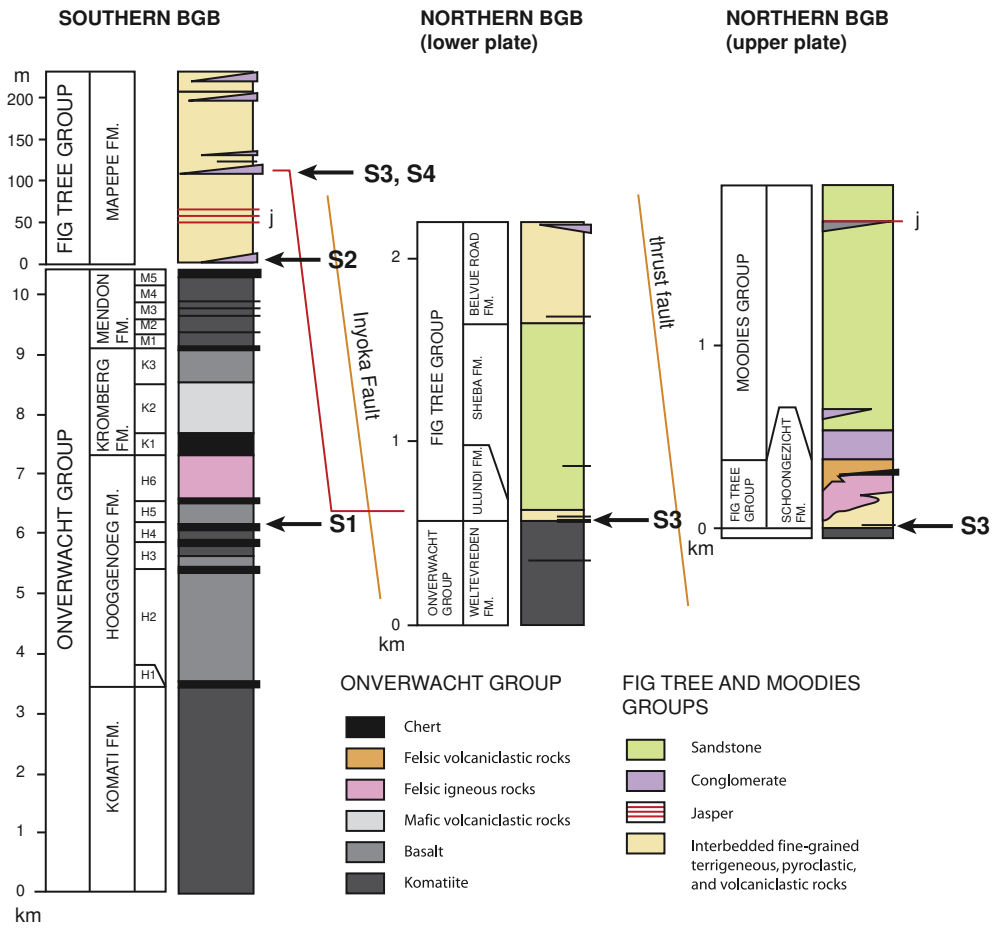

Fig. 1. Stratigraphy of the Onverwacht Group and Fig Tree Group, Barberton Greenstone Belt (BGB), South Africa (after Lowe et al., 2003). Spherule beds are indicated by S1–S4 throughout the sections of the Hooggenoeg Formation and the Mapepe Formation. The southern part of the BGB contains the Songimvelo Block (Lowe et al., 1999), south of the Granville Grove Fault. The northern part of the BGB contains areas north of the Inyoka Fault.

Rock samples were collected from spherule beds S2, S3, and S4 during the 2003 Astrobiology field excursion (organized by D. Lowe and G. Byerly) (Lowe and Byerly, 2003). Sample S2 (25°54.557′S, 31°01.009′E) was collected ca. 1 km west along strike from key locality SAF-374 (Lowe et al., 2003). Samples S3 (25°54.897′S, 31°01.134′E) and S4 (25°54.907′S, 31°01.135′E) were collected at the type locality SAF-179 (Lowe et al., 2003). Conventional 30 μm petrographic thin sections were prepared of each sample. After examination by petrographic microscope, areas of interest were cut from the thin sections by diamond wire saw, embedded in an Epotec 301 epoxy mount, and polished using a diamond paste. A total of seven polished slabs (S2: SPH-5, S3: SPH-1, SPH-6, AL-1, S4: SPH-2, SPH-4, SPH-8) were prepared for SIMS analysis and Raman spectroscopy. Samples of spherule bed S2 consist of silicified detritus (Fig. 2a). The individual clasts consist of black chert and volcanic rock material from the underlying Mendon Formation. The succession largely represents sedimentary deposition from large wave currents, and spherules occur only sporadically (Fig. 2b). The few spherules that were observed did not contain any pyrite, so only pyrite grains were selected from a black chert clast (zone 1, Fig. 2c and d), and from the hydrothermal silica matrix (zone 2, Fig. 2e and f). In thin sections from spherule beds S3 and S4, many spherules are observed (Fig. 3), which consist largely of chlorite and quartz. In some cases pyrite grains occur within or line the outer parts of individual spherules (Figs. 3c, and 4a and b), but pyrite is also found scattered throughout the thin sections. In both S3 and S4 large euhedral pyrite grains are observed, which clearly represent later addition of a sulfur source during hydrothermal alteration (Fig. 5).

3. METHODS

3.1. Raman spectroscopy

A Renishaw In Via Raman spectrometer coupled to an Olympus BX61 confocal microscope was used to identify pyrite and other possible sulfide phases (for detailed description of instrument characteristics and analytical settings, see Sforna et al., 2014). Measurements were made through a 50× objective in static mode (fixed at

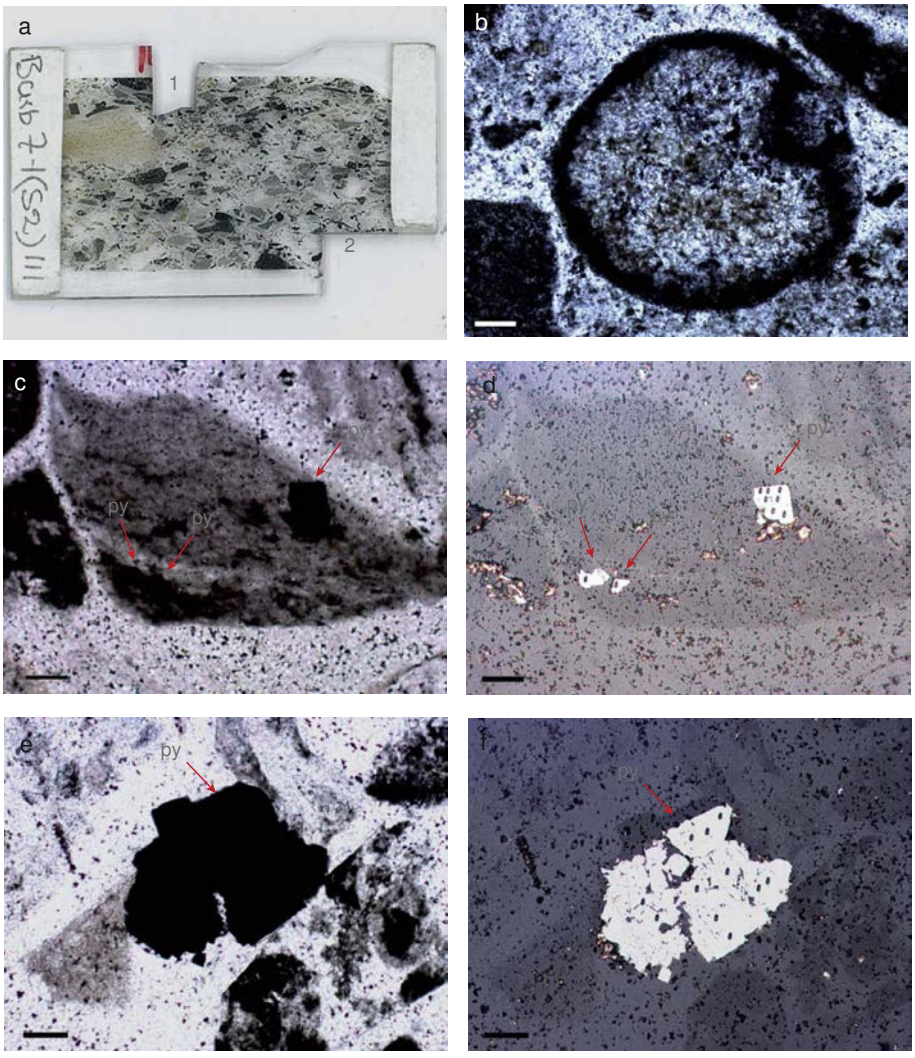

Fig. 2. (a) Thin section image of sample SPH-5 of spherule bed S2. The sample consists of silicified detritus, with clasts representing black chert and volcanic deposits of the underlying Mendon Formation. Two zones were cut out, one representing a black chert clast (zone 1), and one representing the silicified matrix (zone 2). (b) Transmitted light image of a spherule containing an opaque rutile-rich rim. Spherules are rare in bed S2, and occur disseminated throughout the rock matrix. (c) Transmitted light image showing a black chert clast in zone 1, consisting of fluffy carbonaceous grains embedded in finely laminated quartz. Closely associated with the carbonaceous phase are two small pyrite grains and one larger aggregate of pyrite grains. (d) Reflected light image showing the pyrite grains and the locations of ion probe analyses. (e) Transmitted light image showing zone 2 consisting of a large aggregate of small pyrite grains within a silicified zone of the sample. (f) Transmitted light image showing the locations of ion probe analyses. In all panels the scale bar is 100 μm.

1150 cm^{-1}) for 2 × 20 s running time, using a 514 nm laser (on-sample intensity of ca. 0.4 mW). Pyrite was identified with 337, 372, and 425 cm^{-1} Raman peaks by direct comparison with pyrite standard R070173 from the RRUFF online database. Raman analysis was performed within SIMS pits to ensure that each isotope analysis was actually made in a pyrite crystal (Fig. 4).

3.2. Secondary ion mass spectrometry (SIMS)

Polished rock thin section samples were mounted in 25 mm diameter epoxy blocks. Subsequently, a section was cut from these blocks and gold-coated before co-mounting with a set of epoxy-embedded sulfide standards. These standards include the S-MDF pyrites Balmat ($\delta^{34}S = +15.1 \pm 0.2‰$) and Ruttan ($\delta^{34}S = +1.2 \pm 0.1‰$) (Crowe and Vaughan, 1996), as well as S-MIF pyrite 248474 ($\delta^{34}S = +1.99 \pm 0.36‰$, $\Delta^{33}S = 3.31 \pm 0.38‰$) from a ca. 3.7–3.8 Ga banded iron formation of the Isua Greenstone Belt, Southern West Greenland (Whitehouse, 2013). The $\delta^{34}S$ and $\delta^{33}S$ values of sample spots were calibrated relative to the Ruttan reference pyrite, since there is a discrepancy in literature values for Balmat (Crowe and Vaughan, 1996; Cabral et al., 2013; Whitehouse, 2013). Pyrite from banded iron formation GGU 248474 (Isua Greenstone Belt, SW Greenland) was used as a monitor for $\Delta^{33}S$ measurements. Measurements of ^{32}S, ^{33}S, and ^{34}S were made in multicollector mode using the Cameca IMS 1280 ion microprobe at the NordSIMS facility of the Swedish Museum of Natural History, Stockholm. In order

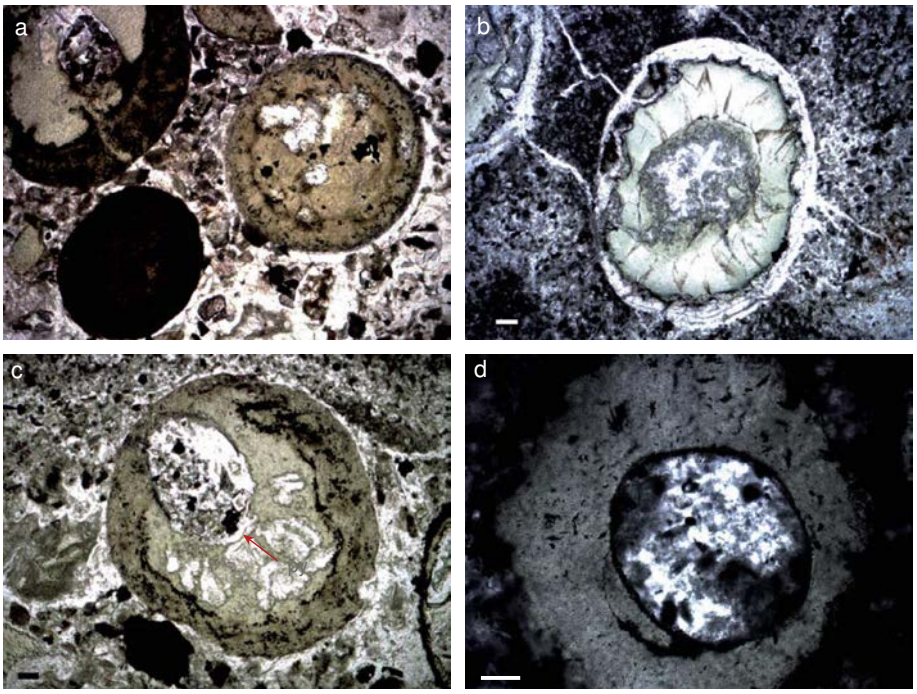

Fig. 3. Transmitted light images of individual spherules: (a) Spherules in bed S3 consisting primarily of chlorite, with small circular cavities filled with quartz. (b) Spherule in bed S3 showing a quartz-filled center, and a larger chlorite layer. (c) Spherule in bed S3 consisting mainly of chlorite, containing some small pyrite grains. (d) Spherule from bed S4, showing a similar chlorite filling and a quartz-filled center. Scale bars in all panels are 100 μm.

to remove the gold coating on the sample surface a 25×25 μm rastered area was pre-sputtered for 90 s, followed by analysis. Sulfur isotopes were analyzed as S^- ions produced by bombardment with a 2.5 nA intensity critically focused (Gaussian) primary Cs^+ beam (operated at 10 kV). Charge compensation during analysis was achieved with a low energy electron gun. The analytical pits were 10 μm in diameter. A 2500 μm field aperture was used corresponding to a field of view on the sample of 30×30 μm (magnification 90×), and analyses were made at a mass resolving power (M/ΔM) of 4860, sufficient to resolve $^{33}S^-$ from $^{32}S^1H^-$. Typical ion intensities of 9×10^8 counts per second (cps) were obtained on $^{32}S^-$. On small grains a single SIMS spot analysis was obtained, while on some larger euhedral sulfides several spot analyses were made. Sulfur isotopic ratios are calculated using equations 1 and 2, and are presented in conventional delta notation in per mil (‰) units relative to CDT. Standard bracketing was achieved before and after each set of 6 sample spot analyses. The average external reproducibility, as estimated from repeated measurements of the sulfur standards, was generally below 0.3‰ for $\delta^{33}S$, 0.2‰ for $\delta^{34}S$, and 0.3‰ for $\Delta^{33}S$ (2 std.dev.).

4. RESULTS

Pure pyrite grains that were identified in the thin sections were further divided into a few large euhedral crystals (ca. 300–600 μm) and smaller crystals (<200 μm). The euhedral pyrite crystals were used as a point of reference during the SIMS analytical sessions, and many individual point analyses were performed on them. For these large crystals only the average values are reported (Fig. 5). Examples of typical analysis spots are shown in Fig. 4a–c. In spherule bed S3, a large zoned pyrite grain was identified (Fig. 4d), and many SIMS analyses were carried out on the centre (zone A), first growth zone (zone B), and outer rim (zone C). All SIMS spot analyses of spherule beds S2, S3, and S4 are listed in Table S1. There is no correlation observed between ion count rate (displayed as the ratio of ion counts on the sample and ion counts on a pyrite standard) and isotope ratios $^{33}S/^{32}S$ and $^{34}S/^{32}S$ (Fig. S1). Measurements with relative count rates against reference pyrite below 0.5 have been excluded from the dataset, assuming that such values indicate that a non-pyrite or even a non-sulfide target was (partially) hit by the ion beam. Some pyrite grains contain small impurities, such as chalcopyrite (Figs. 4e and f and 5c) or anatase (Fig. 4g). The effect on isotope analysis of chalcopyrite is shown in Fig. 5d. A difference in $\delta^{34}S$ of ca. 4‰ is observed between chalcopyrite and pyrite. This could represent a real isotopic difference between the two sulfide phases, or it represents a mineral matrix effect that is introduced during mass-dependent instrumental fractionation. Raman spectroscopic analysis of SIMS pits (Fig. 4h) was used to identify a chalcopyrite matrix, and these analytical points were removed from the dataset.

Spherule bed S2 contains two types of pyrite grains; one type that only displays S-MIF ($\Delta^{33}S = 0$ to +2.0‰) and the other type that only displays S-MDF ($\delta^{34}S = -4.0$ to 0.1‰) (Fig. 6a). The observed sulfur isotope ratios thus appear to confirm that the studied pyrite grains in S2 are all derived from either erosional clasts of the Mendon Formation or

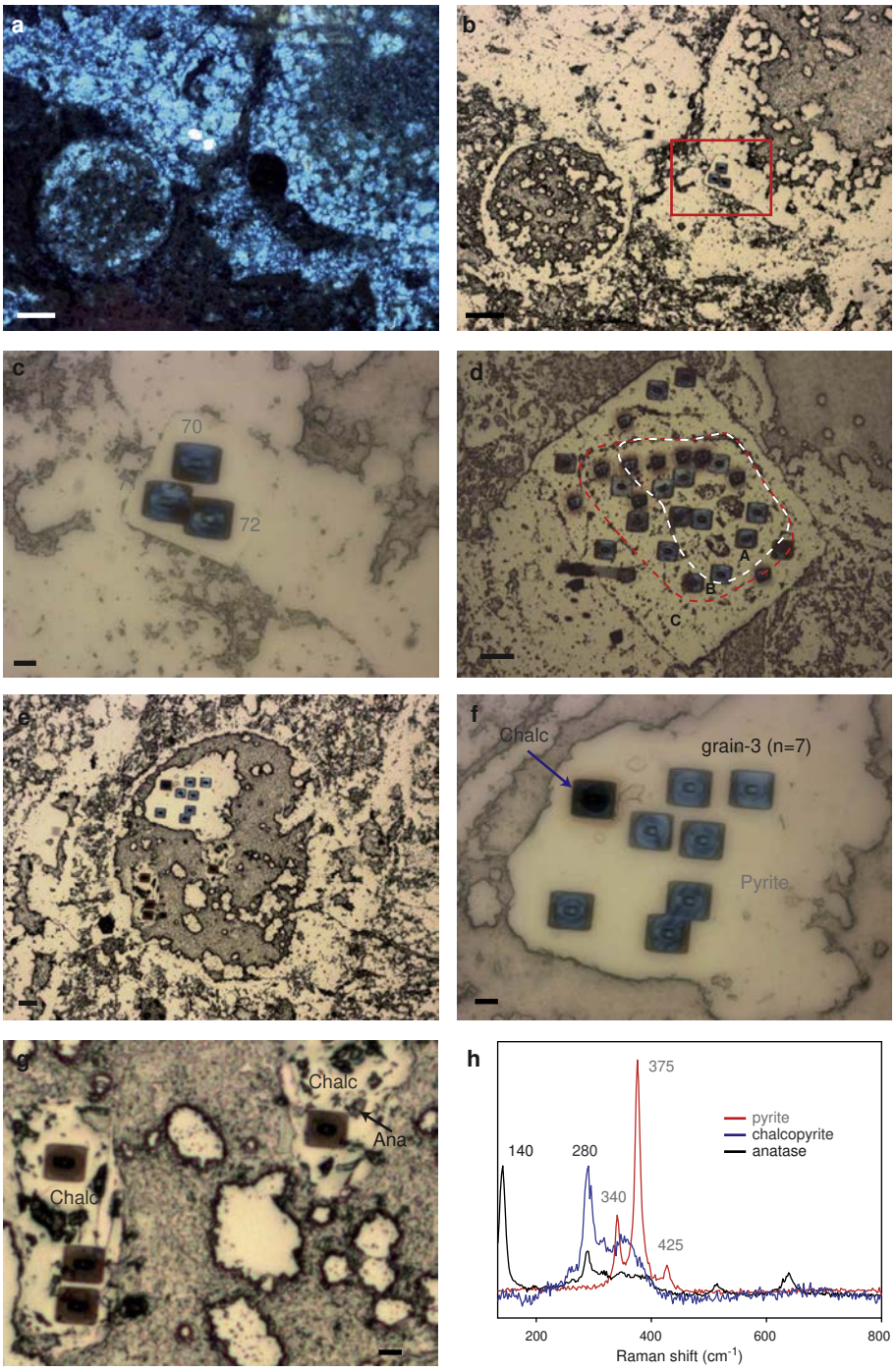

Fig. 4. (a) Example of SIMS analysis on a pyrite grain within a polished mount of spherule bed S3, sample SPH6. Transmitted light image showing a small round spherule (left) and the rim of a large spherule (right). Hydrothermal fluids caused permineralization of the spherules, leading to blue–grey euhedral quartz grains. Scale bar is 100 μm. (b) Reflected-light image showing the location of a pyrite grain with three ion probe pits. (c) Zoom-in on pyrite grain showing the ion probe pits of points 70, 71 and 72. For each pit a 25 μm pre-sputtering rectangle is visible, as well as the 10 μm area of analysis. Scale bar is 15 μm. (d) Zoned pyrite crystal in spherule bed S3, sample AL-01. Ion probe pits cover the entire surface from center to rim. Scale bar is 50 μm. (e) Reflected light image of sample SPH6 of spherule bed S3, showing a spherule structure containing several sulfide grains. Scale bar is 50 μm. (f) Zoom-in on upper sulfide grain, shown in (e). Raman spectroscopy in all ion probe pits confirmed that the grain is pyrite. However, one small region represents chalcopyrite. Scale bar is 15 μm. (g) Zoom-in on lower sulfide grains, shown in (e). Raman spectroscopy confirmed that these grains are chalcopyrite. The grain on the right also includes small crystals of anatase. Scale bar is 15 μm. (h) Raman spectra of pyrite, chalcopyrite, and anatase. Spectra are obtained in ion probe pits shown in (f) and (g). (For interpretation of the references to color in this figure legend, the reader is referred to the web version of this article.)

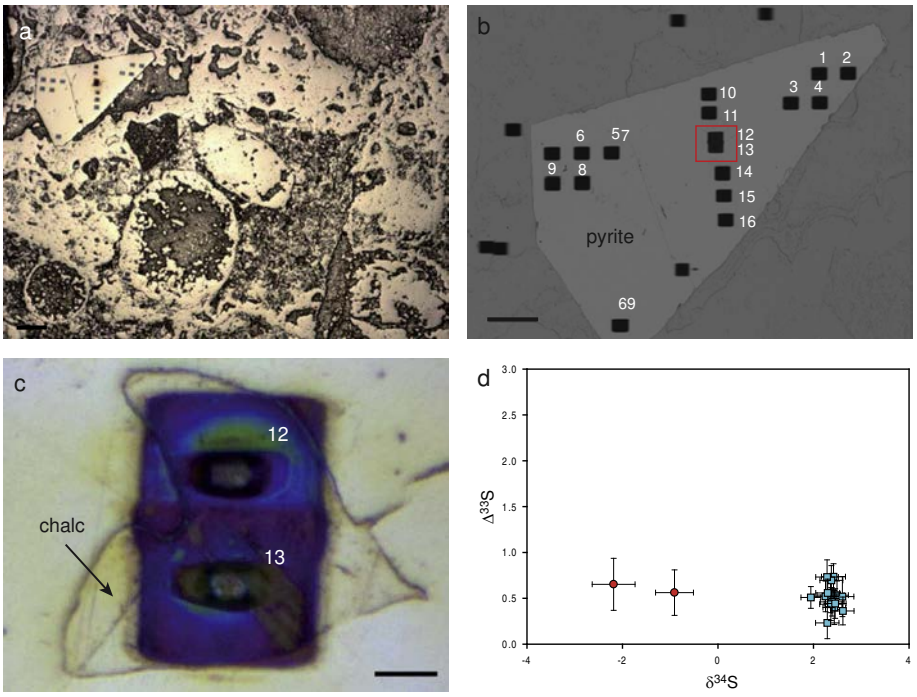

Fig. 5. (a) Reflected light image of a large euhedral pyrite crystal in sample SPH-6 of spherule bed S3. Scale bar is 100 μm. (b) Electron microscope image (secondary electrons) of the same pyrite crystal, showing the exact locations of the ion probe pits. Scale bar is 100 μm. (c) Reflected light image of the red zone shown in (b). SIMS analyses 12 and 13 were obtained from a small chalcopyrite inclusion. Scale bar is 10 μm. (d) Sulfur isotope results of all analyses, showing a significant mass-dependent matrix effect for the two analyses on the chalcopyrite inclusion. (For interpretation of the references to color in this figure legend, the reader is referred to the web version of this article.)

from a sulfur source that was introduced at a later stage during hydrothermal alteration. In this bed there are no indications of an impact-related sulfur source. In contrast, pyrite grains from spherule bed S3 appear to describe a unique trend (Fig. 6c) that reflects mixing between a distinct S-MIF end-member ($\delta^{34}S = +10‰$, $\Delta^{33}S = +2‰$) and the juvenile mantle reservoir ($\delta^{34}S = 0‰$, $\Delta^{33}S = 0‰$). This mixing trend is also observed in the zoned crystal shown in Fig. 4d. The centre (zone A) of this crystal appears to have preserved the S-MIF end-member, while the outer zones B and C have mantle values (Fig. 6d). A similar trend towards this distinct S-MIF end-member, although less well defined, is observed in pyrite grains of spherule bed S4 (Fig. 6b). Overall, these trends suggest that spherule beds S3 and S4 retained a primary sulfur component that may be related to the impact-origin of these rocks.

5. DISCUSSION

5.1. Comparison with other rocks of the Mapepe Formation and underlying Mendon Formation

Philippot et al. (2012) showed that pyrites in felsic ash layers in the Mapepe Formation of the Barberton Greenstone Belt show a negative $\Delta^{33}S/\delta^{34}S$ trend (Fig. 7a). This trend, which is referred to as the Felsic Volcanic Array (FVA) has been attributed to an episode of intense volcanic SO_2 discharge into the atmosphere. Many pyrites in barite deposits of the Mapepe Formation show strongly negative $\delta^{34}S$ values, which can be attributed to mass-dependent sulfur isotope fractionation caused by microbial and/or abiologic sulfate-reduction (MDF-SR) (Shen et al., 2001, 2009; Philippot et al., 2007; Ueno et al., 2008; Philippot et al., 2012; Roerdink et al., 2013). Philippot et al. (2012) concluded that the entire range of observed $\delta^{34}S$ and $\Delta^{33}S$ values of these barite-deposit pyrites can be explained by different degrees of mixing between a photochemical S^0 source related to the FVA and sulfides derived from MDF-SR (Fig. 7b). In contrast, komatiitic volcanic units and deep water carbonaceous cherts at the top of the underlying Mendon Formation do not shown any significant negative shift in $\delta^{34}S$, and do not follow this FVA. Rather, they overlap with the generally observed positive trend in Archean sediments (Fig. 7a). The slope of this trend varies throughout the Archean, and according to depositional environment (Ono et al., 2003, 2009a,b; Kamber and Whitehouse, 2007; Kaufman et al., 2007; Ueno et al., 2008; Zerkle et al., 2012). Particularly in late Archean sediments an overall slope of ca. $\Delta^{33}S/\delta^{34}S = 0.9$ is observed (Ono et al., 2003, 2009a,b; Kamber and Whitehouse, 2007; Kaufman et al., 2007).

Recently, Roerdink et al. (2013) reported sulfur isotope compositions of pyrites in barite deposits, volcanoclastic deposits, conglomerates, cherts, and dolomites of the Mapepe Formation (Fig. 7c). They observed a comparable range in sulfur isotopic ratios as Philippot et al. (2012) with the exception of the strongly anomalous FVA values in volcanic ash layers. They also noted a specific difference in isotopic trends between barite-rich sediments and barite-free sediments, and concluded that most of the observed

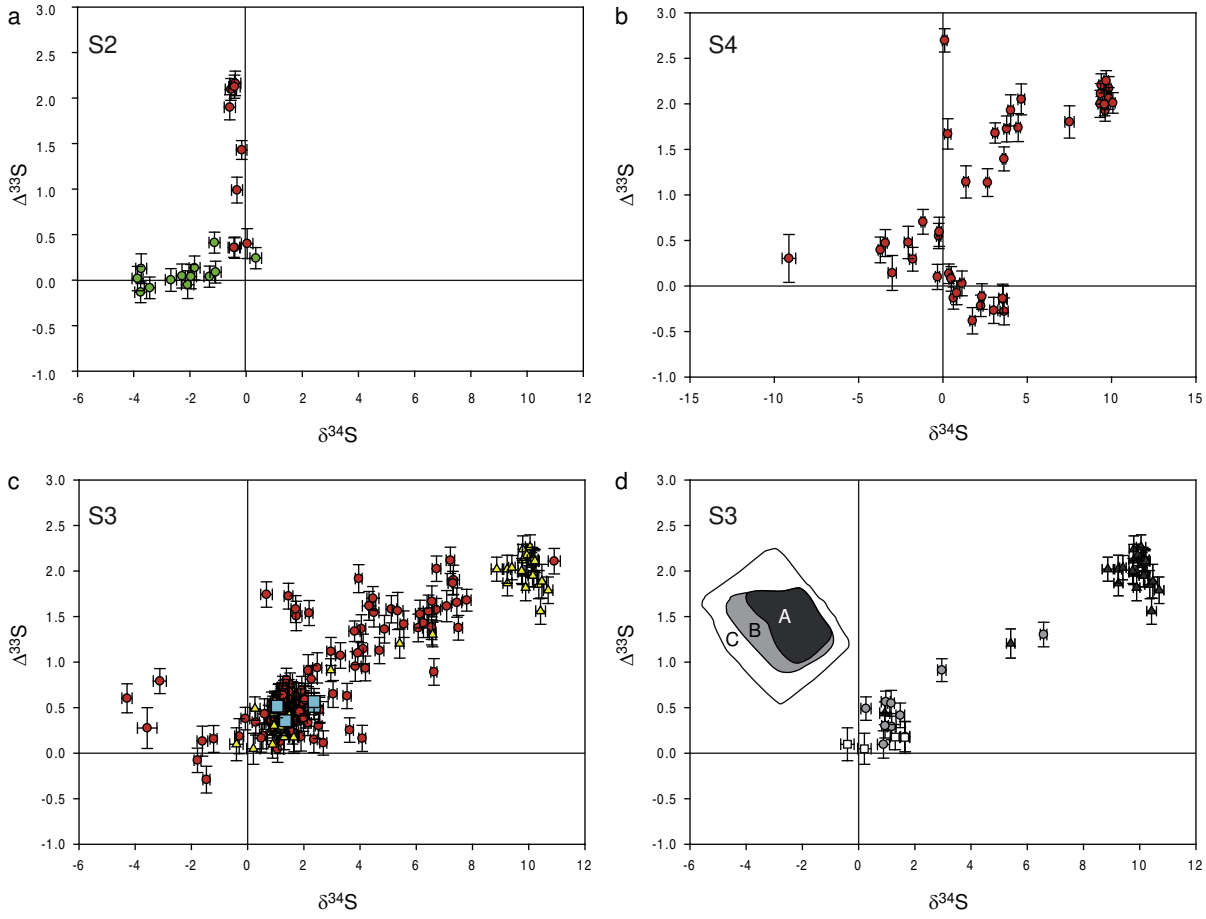

Fig. 6. S-MDF ($\delta^{34}S$) and S-MIF ($\Delta^{33}S$) of all point analyses on pyrites in spherule bed samples. All data points shown in these figures are listed in Table S1. (a) Spherule bed S2; pyrite grains occurring in a black chert clast (red circles) and pyrite grains occurring in the silica matrix (green circles). (b) Spherule bed S4; pyrite grains (red circles). (c) Spherule bed S3; pyrite grains (red circles), large euhedral pyrite grains used as reference (blue squares), and a zoned pyrite crystal (yellow triangles). (d) Detailed analyses of the zoned pyrite grain from spherule bed S3, shown in Fig. 4d. A clear difference is observed between the center (zone A, black triangles), and the two outer rims (zones B, grey circles, and C, white squares). (For interpretation of the references to color in this figure legend, the reader is referred to the web version of this article.)

S-MDF and S-MIF values in the Mapepe Formation can be explained by shifts in environmental conditions in the depositional basin rather than mixing of products of primary atmospheric processes.

The important observation is made here that the S-isotope compositions in pyrites of spherule bed S3 (Fig. 7) – and to a lesser extent spherule bed S4 – show an anomalous trend that is completely different from the FVA trend (Philippot et al., 2012), cannot be explained by the mixing wedge proposed by Philippot et al. (2012), and cannot be explained by the environmental controls that were proposed by Roerdink et al. (2013). Only some large euhedral pyrite crystals (Fig. 5) and the outer rims of the zoned crystal (regions B and C) in spherule bed S3 (Fig. 4d) show values that are shifted to low $\delta^{34}S$ and $\Delta^{33}S$, representing late stage mixing. For spherule bed S2 the pyrites found in the black chert clast (Fig. 2c and d) have $\delta^{34}S$ and $\Delta^{33}S$ values (Fig. 6a) directly overlapping with those of carbonaceous cherts of the underlying Mendon Formation (Fig. 7a, Philippot et al., 2012). Pyrites from the silica matrix (Fig. 2e and f) fall in the general mixing range defined by Philippot et al. (2012) and Roerdink et al. (2013). It is concluded that pyrites of spherule beds S3 and S4 describe a unique trend that likely represents primary deposition of an impact dust cloud and carries an S^0 component of atmospheric SO_2 photochemistry.

5.2. Possible sources of sulfur preserved in spherule beds

The observed S-MIF anomaly is only observed in a few small pyrite grains, or in the center of larger zoned pyrites. Clearly, the atmospheric photochemical S^0 aerosol products that carried this anomalous isotopic trend, and that were incorporated into the dust cloud, only represent a small fraction of the total sulfide inventory in the spherule bed deposits. The spherule beds represent a giant impact. The bolide is estimated to have been ca. 30 km in diameter, causing a crater of ca. 500 km in diameter with a depth of ca. 16 km (Krull-Davatzes et al., 2014). On hitting the Earth's surface it would have released an enormous amount of water vapor, and would have excavated through sediments, the oceanic crust, into the upper mantle

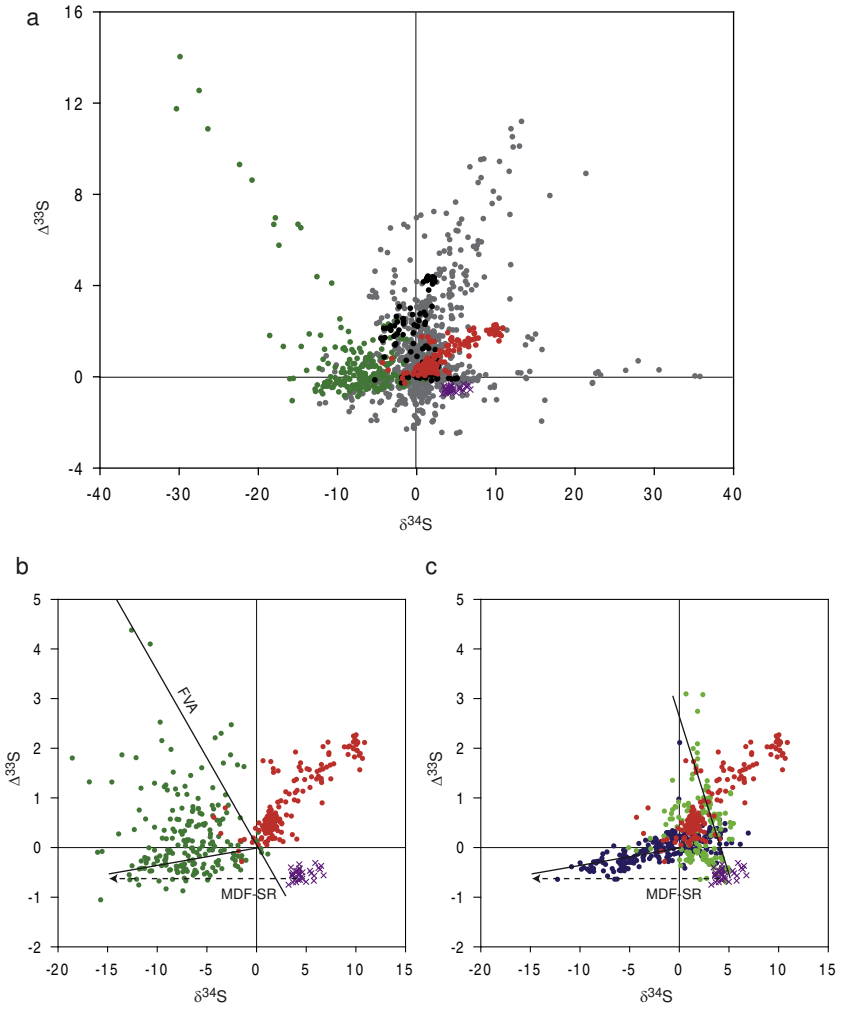

Fig. 7. (a) $\delta^{34}S$–$\Delta^{33}S$ plot of spherule bed pyrites (red circles), compared with pyrites from komatiites and black cherts of the Mendon Formation (black circles) and pyrites from the barite deposits and volcanoclastic ash layers of the Mapepe Formation (green circles) of the Barberton Greenstone Belt (data points from Philippot et al., 2012). Pyrites from the volcanic ash layers define a negative $\Delta^{33}S/\delta^{34}S$ trend (Felsic Volcanic Array, FVA), while many of the pyrites in the barite deposits show a shift to strongly negative $\delta^{34}S$ caused by microbial and/or abiologic mass-dependent sulfate reduction (MDF-SR). The grey circles represent the generally observed Archean Reference Array (ARA). Sulfur isotope composition of sulfate is shown for barite deposits of the Mapepe Formation (purple crosses, data points from Bao et al. (2007) and Roerdink et al. (2012). (b) Zoom-in of Fig. 4a, showing the mixing wedge defined by the FVA and MDF-SR. (c) Sulfur isotopic composition data from Roerdink et al. (2013) for the Mapepe Formation. A clear difference is seen between pyrites in barite-rich sediments (blue circles) and barite-poor sediments (light green circles). A trend of MDF-SR is observed that is similar to that reported by Philippot et al. (2012). (For interpretation of the references to color in this figure legend, the reader is referred to the web version of this article.)

(Krull-Davatzes et al., 2014). The resulting dust cloud was globally distributed (Lowe et al., 2003), and consisted of rock melt particles and condensation particles, largely representing cherty sediments, basaltic rock and meteorite material. Only a small fraction of this dust cloud consisted of micron- and sub-micron-size particles that would have remained in the atmosphere for several months (Toon et al., 1997). Any atmospheric photochemical S^0 aerosols would thus mix with the sulfur component already present in the dust cloud. This dust-derived sulfur largely represents basaltic rock and meteorite material, and would thus carry a mantle-type sulfur isotopic signature. Indeed, it is seen that the mixing trend of the observed S-MIF anomaly crosses the origin in a $\delta^{34}S$–$\Delta^{33}S$ plot (Fig. 6b–d). Another sulfur source that would dilute the S-MIF anomaly of S^0 aerosol products is represented by the sulfide products of microbial and/or abiologic sulfate-reduction (MDF-SR). The Archean ocean episodically contained concentrations of sulfate that were high enough to cause precipitation of barite deposits (Huston and Logan, 2004; Philippot et al., 2012) and isotopic evidence of contemporaneous MDF-SR has been presented (Ohmoto et al., 1993; Roerdink et al., 2012, 2013; Shen et al., 2001, 2009; Ueno et al., 2008). One such short duration episode occurred 3.26–3.24 Ga ago, and overlapped with the deposition of spherule bed S3 (Fig. 1). Isotopic evidence for MDF-SR in sulfides of barite-rich rocks in the Mapepe Formation (Philippot et al., 2012; Roerdink et al., 2012, 2013)

(Fig. 7) further supports the possibility that a fraction of the sulfur inventory in spherule bed S3 could be derived from a seawater sulfate source. Indeed, some individual pyrite grains that were measured by SIMS showed a shift towards negative $\delta^{34}S$ (Fig. 6b and c). Overall, it can be concluded that sulfur from several sources was incorporated into the spherule beds, and aerosol products of high-altitude atmospheric photochemical reactions only formed a very small fraction of this total sulfur inventory. Nevertheless, in situ analysis of individual pyrite grains using SIMS showed that a specific anomaly could be identified and is preserved in the rock record.

5.3. Photochemistry of atmospheric SO_2 and the general Archean $\delta^{34}S$–$\Delta^{33}S$ trend

The molecule SO_2 has two dominant adsorption bands in the UV-region, one at 190–220 nm and the other at 250–330 nm (Heicklen et al., 1980). In the region 190–220 nm, absorption is assigned to the electronic transition C^1B_2-X^1A_1, and photo-dissociation of SO_2 proceeds by the reaction: $SO_2 + h\nu \rightarrow {}^*SO_2 \rightarrow SO + O$ (where $^*SO_2$ represents electronically excited SO_2). Subsequent photolysis of SO proceeds by the reaction: $SO + h\nu$ (<230 nm) $\rightarrow S + O$, while atomic oxygen reacts with residual SO_2 to form SO_3 ($SO_2 + O \rightarrow SO_3$). Theoretical calculations and experimental studies have shown that SO_2 photolysis in the 190–220 nm range is associated with an SO_2 isotopologue self-shielding effect and leads to S^0 products with positive $\delta^{34}S$ and $\Delta^{33}S$ that form an isotopic compositional array of ca. $\Delta^{33}S/\delta^{34}S \approx 0.06$–$0.14$ (Lyons, 2007, 2009; Ono et al., 2013; Whitehill and Ono, 2012) (Fig. 8a). The $\delta^{34}S$ of the photolysis product S^0 increases with increasing SO_2 pressure, and the slope $\Delta^{33}S/\delta^{34}S$ increases with decreasing pressures of a nitrogen bath gas (Ono et al., 2013). At a certain maximum SO_2 pressure (at ca. 10 mbar SO_2) the self-shielding effect reaches saturation and $\delta^{34}S$ does not further increase. At even higher SO_2 pressures (>30 mbar SO_2), such as in the experiments of Masterson et al. (2011) using He as a bath gas, the SO_2 itself behaves as a bath gas and there is a diminution of the S-MIF signal.

In the region 250–330 nm of the spectrum absorption is attributed to the B^1B_1-X^1A_1 electronic transition, and photo-excitation of SO_2 proceeds by the reaction: $SO_2 + h\nu \rightarrow {}^*SO_2$. Photolysis does not occur, and instead photo-oxidation through self-reaction with ground state SO_2 takes place: $^*SO_2 + SO_2 \rightarrow SO_3 + SO$. The produced SO can react with other SO molecules ($SO + SO \rightarrow S + SO_2$), or react with SO_3 ($SO + SO_3 \rightarrow 2SO_2$). Photochemical experiments in the 250–330 nm region (Whitehill and Ono, 2012; Whitehill et al., 2013) showed that the product S^0 has a relatively weak positive $\delta^{34}S$, but strongly positive $\Delta^{33}S$ (Fig. 8a). The highest S-MIF signals are produced at relatively low SO_2 pressure, confirming that isotopologue self-shielding is not the dominant effect. Rather, it is suggested that differences in intersystem crossing (ISC) rates from an initially excited singlet state to a reactive or dissociative triplet state is responsible. The excited-state SO_2 which carries the S-MIF signature is difficult to preserve, and

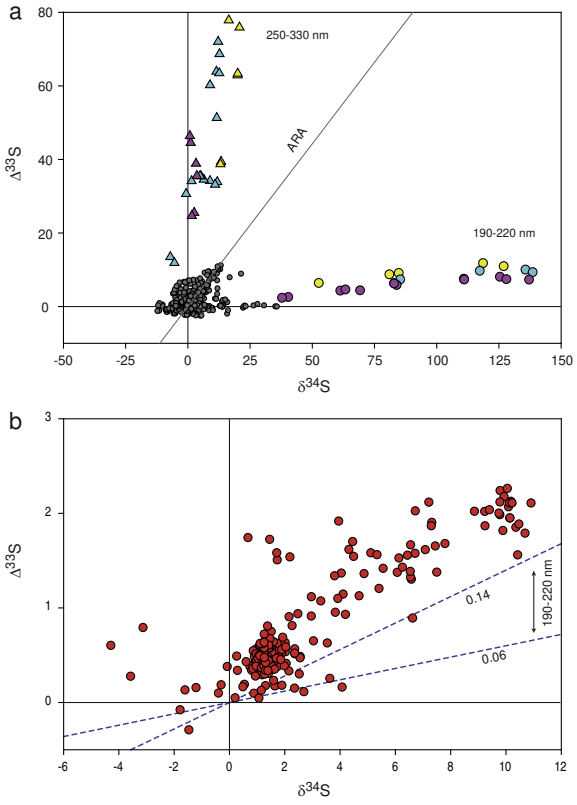

Fig. 8. (a) Experimental data from Ono et al. (2013) showing $\delta^{34}S$ and $\Delta^{33}S$ values of S^0 products from SO_2 photolysis in the 190–220 nm spectral range (circles), and experimental data from Whitehill et al. (2013) showing $\delta^{34}S$ and $\Delta^{33}S$ values of S^0 products from SO_2 photoexcitation in the 250–330 nm spectral range (triangles). For Ono et al. (2013) experimental results at different bath gas (nitrogen) pressures are shown; purple circles at $pN_2 =$ 1 bar, blue circles at $pN_2 = 0.5$ bar, and yellow circles at $pN_2 =$ 0.25 bar. For Whitehill et al. (2013) experimental results at different total pressure are shown; purple triangles at $P = 1013$ mbar, blue triangles at $P = 506$ mbar, yellow triangles $P = 253$ mbar. Other trends shown in this figure are the Archean Reference Array (ARA) with a slope of $\Delta^{33}S = 0.9\ \delta^{34}S$, and the Felsic Volcanic Array (FVA) with a slope of $\Delta^{33}S = -0.4\ \delta^{34}S$. (b) The spherule bed S3 (red circles) defines a slope of $\Delta^{33}S = 0.23\ \delta^{34}S$. This strongly deviates from the ARA trend but is rather close to the 0.06–0.14 slopes observed in the experiments of Ono et al. (2013) and Whitehill and Ono (2012). (For interpretation of the references to color in this figure legend, the reader is referred to the web version of this article.)

therefore unlikely to be recorded into the rock record. However, it has been shown (DeWitt et al., 2010) that UV radiation of SO_2 in the presence of methane can produce organosulfur aerosols, which could potentially act as an exit channel for this S-MIF signal. Also the excited-state SO_2 could react with small organic molecules such as C_2H_2 to form organosulfur aerosols (Whitehill and Ono, 2012).

The SO_2 photolysis reaction in the 190–220 nm adsorption range has been generally seen as the main source of atmospheric S-MIF in the Archean (Farquhar et al., 2000; Pavlov and Kasting, 2002; Lyons, 2007; Danielache et al., 2008; Masterson et al., 2011). However, in order to

explain the strongly positive $\Delta^{33}S$ values (>2.5‰) that are often observed, a very high atmospheric SO_2 column density should have been maintained throughout the Archean. Moreover, the observed positive $\Delta^{33}S$ values should be associated with very strongly positive $\delta^{34}S$ values. Clearly the ARA is at odds with theoretical and experimental studies of SO_2 photolysis in the 190–220 range (Fig. 8a). Lyons (2009) presented various explanations for a diminution of $\delta^{34}S$, including chemical and biogenic S-MDF effects during elemental sulfur formation in the atmosphere, or aqueous phase reactions of HS^- with Fe^{2+} and FeS in the oceans. Whitehill and Ono (2012) suggested that a mixture of sulfur products from SO_2 photo-excitation in both the 190–220 nm and the 250–330 nm absorption bands could explain the specific trend that is observed in sulfide deposits throughout the Archean. This could be attained if the atmosphere contained methane, leading to the formation of organosulfur aerosols as an additional exit channel (DeWitt et al., 2010) and the enhanced preservation of the signature of SO_2-photo-excitation in the 250–330 nm range. Alternatively, the presence of an organic haze layer (Sagan and Chyba, 1997; Haqq-Misra et al., 2008) could have specifically blocked the lower part of the solar spectrum (Wolf and Toon, 2012), which would have reduced the rate of direct SO_2-photolysis in the 190–220 nm range and at the same time would have provided an environment rich in alkanes and C_2H_2 in which the signature of SO_2-photo-excitation in the 250–330 nm range could be preserved (Whitehill and Ono, 2012).

5.4. Impact-induced $\delta^{34}S$–$\Delta^{33}S$ trend in early Archean spherule beds

The overall trend $\Delta^{33}S/\delta^{34}S = 0.23$ that is observed in the pyrite grains in spherule bed S3, and to a lesser extend S4, deviates significantly from the ARA, but is relatively close to the theoretical and experimental trend for SO_2-photolysis in the 190–220 nm spectral range ($\Delta^{33}S/\delta^{34}S \approx 0.06$–$0.14$) (Lyons, 2007, 2009; Ono et al., 2013; Whitehill and Ono, 2012) (Fig. 8b). Since this trend is specifically observed in spherule beds, it is likely that it is related to an impact-induced disturbance in the atmosphere. The impact of a large bolide can cause the ejection of enormous amounts of water, gases, and rock dust, leading to an optically thick layer in the atmosphere (Toon et al., 1997) that blocks radiation in both the UV and visible range (Pierazzo and Artemieva, 2012). Under such circumstances any photochemical reactions would be largely prevented in the lower part of the atmosphere, and it is likely that the dust itself incorporated S-MIF products that were produced by a photolytic process higher up in the atmosphere.

In the modern atmosphere a specific S-MIF signature is typically observed at high altitude after episodes of large volcanic eruptions (Savarino et al., 2003; Baroni et al., 2007, 2008). Stratospheric sulfate aerosols (SSA) deposited in polar ice recorded an S-MIF signature that appears to be specifically linked to SO_2-photolysis in the 190–220 nm range (Ono et al., 2013). This effect is generally explained by an increased SO_2 column density in the stratosphere causing an isotopologue self-shielding effect. It is possible that the Archean spherule beds recorded a similar upper-atmosphere S-MIF signature that was generated exclusively by SO_2-photolysis. At such high altitude in the Archean atmosphere methane and organic haze gases such as alkanes C_2H_2 were probably relatively scarce, and S-MIF products of SO_2 photoexcitation in the 240–350 nm range were not preserved. It was shown by Ono et al. (2013) that the ratio $\Delta^{33}S/\delta^{34}S$ of product S^0 in a SO_2-photolysis reaction increases when the bath gas (nitrogen) pressure decreases (Fig. 8a). The observed $\Delta^{33}S/\delta^{34}S = 0.23$ in the spherule beds could thus indicate that SO_2-photolysis took place at high altitude under very low pressure conditions.

Based on $\delta^{34}S$ and $\Delta^{33}S$ measurements alone it is difficult to establish if these spherule beds indeed uniquely recorded a high-altitude SO_2-photolysis effect in the 190–220 nm range, or also involved other atmospheric photochemical processes and/or later mass-dependent chemical effects. For instance, the S-MIF signal that is recorded in sediments also depends on the relative photochemical exit channels of SO_3 and S^0 (Zerkle et al., 2012; Kurzweil et al., 2013). An impact-induced shift in atmospheric redox conditions could have favored preservation of S^0 over SO_3 and thus have diminished the positive S-MIF signal. Future measurements of ^{36}S in these spherule bed pyrites could possibly confirm an isotopologue self-shielding effect. The general Archean reference array has a $\Delta^{36}S/\Delta^{33}S$ ratio between −0.9 and −1.5 (Kaufman et al., 2007; Zerkle et al., 2012), SO_2-photolysis in the 190–220 nm range a ratio of -4.6 ± 1.3 (Ono et al., 2013), and SO_2-photoexcitation in the 240–350 nm range a ratio between 1.12 and 2.25 (Whitehill et al., 2013). Both photochemical processes show a dependence on both pSO_2 and bathing gas pressure. A detailed quadruple sulfur isotope study on these spherule beds pyrites could therefore potentially confirm or reject SO_2-photolysis as a source reaction.

6. CONCLUSIONS

The sulfur isotope composition was studied of pyrite grains from three spherule beds in the 3.24 Ga Mapepe Formation, Fig Tree Group, Barberton, South Africa. Each of these deposits represents a settling dust cloud after a large meteorite impact event. Since this material reached high altitudes in the atmosphere, it could have adsorbed sulfur aerosols and therefore have recorded specific photolytic isotope anomalies. The sample of spherule bed S2 contained only very few spherules, and pyrite grains in this rock either display a sulfur isotope signature similar to that found in black cherts in the underlying Mendon Formation, or represent a sulfur source that was introduced at a later stage during hydrothermal alteration. In contrast, the sulfur isotope compositions in pyrites of spherule bed S3 – and to a lesser extent spherule bed S4 – show an anomalous trend $\Delta^{33}S/\delta^{34}S = 0.23$, that reflects mixing between a distinct S-MIF end-member ($\delta^{34}S = +10‰$, $\Delta^{33}S = +2‰$) and the juvenile mantle reservoir ($\delta^{34}S = 0‰$, $\Delta^{33}S = 0‰$). This trend significantly differs from all other sediments in the Mendon and Mapepe Formations, and also differs from the general Archean array (ARA). It appears that this trend more closely overlaps with the theoretical and experimental

trend for SO_2-photolysis in the 190–220 nm spectral range ($\Delta^{33}S/\delta^{34}S = 0.06–014$). It is possible that impact dust particles sampled the high, upper layer of the atmosphere where photochemical reactions were dominated by SO_2 isotopologue self-shielding effects.

ACKNOWLEDGMENTS

Samples for this study were collected during the 2003 NASA Astrobiology Institute Field Workshop "Archean Surface Processes", in South Africa. M.A. van Zuilen thanks the organizers D. Lowe (Stanford University) and G. Byerly (Louisiana State University) for field guidance during this workshop. This work was supported by ANR grant eLIFE2 to P. Philippot and Labex UnivEarths to P. Philippot and M.A. van Zuilen. K. Lindén is thanked for technical support during sample preparation. We thank S. Ono, two anonymous reviewers, and Associate Editor F. Moynier for careful and constructive reviews. The Nordsim ion microprobe facility is operated under an agreement with the joint Nordic research cooperation agency, NOS-N. This is Nordsim contribution 371 and IPGP N° 3557.

APPENDIX A. SUPPLEMENTARY DATA

Supplementary data associated with this article can be found, in the online version, at http://dx.doi.org/10.1016/j.gca.2014.07.018.

REFERENCES

Bao H., Rumble, III, D. and Lowe D. R. (1997) The five stable isotope compositions of Fig Tree barites: implications on sulfur cycle in ca. 3.2 Ga oceans. *Geochim. Cosmochim. Acta* **71**, 4868–4879.

Baroni M., Thiemens M. H., Delmas R. J. and Savarino J. (2007) Mass-independent sulfur isotopic compositions in stratospheric volcanic eruptions. *Science* **315**, 84–87.

Baroni M., Savarino J., Cole-Dai J., Rai V. K. and Thiemens M. H. (2008) Anomalous sulfur isotope compositions of volcanic sulfate over the last millennium in Antarctic ice cores. *J. Geophys. Res.* **113**, 1–12.

Byerly G. R., Kröner A., Lowe D. R., Todt W. and Walsh M. M. (1996) Prolonged magmatism and time constraints for sediment deposition in the early Archean Barberton greenstone belt: evidence from the Upper Onverwacht and Fig Tree groups. *Precambr. Res.* **78**, 125–138.

Cabral R. A., Jackson M. G., Rose-Koga E. F., Koga K. T., Whitehouse M. J., Antonelli M. A., Farquhar J., Day J. M. D. and Hauri E. H. (2013) Anomalous sulphur isotopes in plume lavas reveal deep mantle storage of Archaean crust. *Nature* **496**, 490–494.

Crowe D. E. and Vaughan R. G. (1996) Characterization and use of isotopically homogeneous standards for in situ laser microprobe analysis of $^{34}S/^{32}S$ ratios. *Am. Mineral.* **81**, 187–193.

Danielache S. O., Eskebjerg C., Johnson M. S., Ueno Y. and Yoshida N. (2008) High-precision spectroscopy of ^{32}S, ^{33}S, and ^{34}S sulfur dioxide: ultraviolet absorption cross sections and isotope effects. *J. Geophys. Res.* **113**, 1–14.

DeWitt H. L., Hasenkopf C. A., Trainer M. G., Farmer D. K., Jeminez J. L., McKay C. P., Toon O. B. and Tolbert M. A. (2010) The formation of sulfate and elemental sulfur aerosols under varying laboratory conditions: implications for early Earth. *Astrobiology* **10**, 773–781.

Farquhar J., Bao H. and Thiemens M. (2000) Atmospheric influence of Earth's earliest sulfur cycle. *Science* **289**, 756–758.

Glikson A. (2010) Archaean asteroid impacts, banded iron formations and MIF-S anomalies: a discussion. *Icarus* **207**, 39–44.

Haqq-Misra J. D., Domagal-Goldman S. D., Kasting P. J. and Kasting J. F. (2008) A revised, hazy methane greenhouse for the Archean Earth. *Astrobiology* **8**, 1127–1137.

Heicklen J., Kelly N. and Partymiller K. (1980) The photophysics and photochemistry of SO_2. *Rev. Chem. Intermed.* **3**, 315–404.

Huston D. L. and Logan G. A. (2004) Barite, BIFs and bugs: evidence for the evolution of the Earth's early hydrosphere. *Earth Planet. Sci. Lett.* **220**, 41–55.

Kamber B. S. and Whitehouse M. J. (2007) Micro-scale sulphur isotope evidence for sulphur cycling in the late Archean shallow ocean. *Geobiology* **5**, 5–17.

Kaufman A. J., Johnston D. T., Farquhar J., Masterson A. L., Lyons T. W., Bates S., Anbar A. D., Arnold G. L., Garvin J. and Buick R. (2007) Late Archean biospheric oxygenation and atmospheric evolution. *Science* **317**, 1900–1903.

Kröner A., Byerly G. R. and Lowe D. R. (1991) Chronology of early Archaean granite–greenstone evolution in the Barberton Mountain land, South Africa, based on precise dating by single zircon evaporation. *Earth Planet. Sci. Lett.* **103**, 41–54.

Krull-Davatzes A. E., Byerly G. R. and Lowe D. R. (2010) Evidence for a low-O_2 Archean atmosphere from nickel-rich chrome spinels in 3.24 Ga impact spherules, Barberton greenstone belt, South Africa. *Earth Planet. Sci. Lett.* **296**, 319–328.

Krull-Davatzes A. E., Lowe D. R. and Byerly G. R. (2012) Mineralogy and diagenesis of 3.24 Ga meteorite impact spherules. *Precambr. Res.* **196–197**, 128–148.

Krull-Davatzes A. E., Byerly G. R. and Lowe D. R. (2014) Paleoarchean ocean crust and mantle excavated by meteor impact: insights into early crustal processes and tectonics. *Geology* **42**, 635–638.

Kurzweil F., Claire M. W., Thomazo C., Peters M., Hannington M. and Strauss H. (2013) Atmospheric sulfur rearrangement 2.7 billion years ago: evidence for oxygenic photosynthesis. *Earth Planet. Sci. Lett.* **366**, 17–26.

Kyte F. T., Shukolyukov A., Lugmair G. W., Lowe D. R. and Byerly G. R. (2003) Early Archean spherule beds: chromium isotopes confirm origin through multiple impacts of projectiles of carbonaceous chondrite type. *Geology* **31**, 283–286.

Lowe D. R. and Byerly G. R. (1986) Early Archean silicate spherules of probable impact origin, South Africa and Western Australia. *Geology* **14**, 83–86.

Lowe D. R., Byerly G. R. and Heubeck C. (1999) Structural divisions and development of the west-central part of the Barberton Greenstone Belt. In *Geologic Evolution of the Barberton Greenstone Belt, South Africa* (eds. D. R. Lowe and C. R. Byerly). Geological Society of America, Boulder, CO, pp. 37–82, Special Paper 329.

Lowe D.R. and Byerly G.R., (2003), Field Guide to the Geology of the 3.5–3.2 Ga Barberton Greenstone Belt, South Africa: Guidebook prepared for Field Conference, Archean Surface Processes, June 23-July 2, pp. 184.

Lowe D. R. and Nocita B. W. (1999) Foreland basin sedimentation in the Mapepe Formation, southern-facies Fig Tree Group. In *Geologic Evolution of the Barberton Greenstone Belt, South Africa* (eds. D. R. Lowe and G. R. Byerly). Geological Society of America.

Lowe D. R., Byerly G. R., Kyte F. T., Shukolyukov A., Asaro F. and Krull A. (2003) Spherule beds 3.47–3.24 billion years old in the Barberton Greenstone Belt, South Africa: a record of large meteorite impacts and their influence on early crustal and biological evolution. *Astrobiology* **3**, 7–48.

Lyons J. R. (2007) Mass-independent fractionation of sulfur isotopes by isotope-selective photodissociation of SO_2. *Geophys. Res. Lett.* **34**, L22811.

Lyons J. R. (2009) Atmospherically-derived mass-independent sulfur isotope signatures, and incorporation into sediments. *Chem. Geol.* **267**, 164–174.

Masterson A., Farquhar J. and Wing B. A. (2011) Sulfur mass-independent fractionation patterns in the broadband UV photolysis of sulfur dioxide: pressure and third body effects. *Earth Planet. Sci. Lett.* **306**, 253–260.

Ohmoto H., Kakegawa T. and Lowe D. R. (1993) 3.4-Billion-year-old biogenic pyrites from Barberton, South Africa: sulfur isotope evidence. *Science* **262**, 555–557.

Ono S., Eigenbrode J. L., Pavlov A. A., Kharecha P., Rumble, III, D., Kasting J. F. and Freeman K. H. (2003) New insights into Archean sulfur cycle from mass-independent sulfur isotope records from the Hamersley Basin, Australia. *Earth Planet. Sci. Lett.* **213**, 15–30.

Ono S., Beukes N. J. and Rumble D. (2009a) Origin of two distinct multiple-sulfur isotope compositions of pyrite in the 2.5 Ga Klein Naute Formation, Griqualand West Basin, South Africa. *Precambr. Res.* **169**, 48–57.

Ono S., Kaufman A. J., Farquhar J., Sumner D. Y. and Beukes N. J. (2009b) Lithofacies control on multiple-sulfur isotope records and Neoarchean sulfur cycles. *Precambr. Res.* **169**, 58–67.

Ono S., Whitehill A. R. and Lyons J. R. (2013) Contributions of isotopologue self-shielding to sulfur mass-independent fractionation during sulfur dioxide photolysis. *Journal of Geophysical Research: Atmospheres* **118**, 2444–2454.

Pavlov A. A. and Kasting J. F. (2002) Mass-independent fractionation of sulfur isotopes in Archean sediments: strong evidence for an anoxic Archean atmosphere. *Astrobiology* **2**, 27–41.

Philippot P., van Zuilen M., Lepot K., Thomazo C., Farquhar J. and Van Kranendonk M. J. (2007) Early Archean microorganisms preferred elemental sulfur, not sulfate. *Science* **317**, 1534–1537.

Philippot P., van Zuilen M. and Rollion-Bard C. (2012) Variations in atmospheric sulphur chemistry on early Earth linked to volcanic activity. *Nat. Geosci.* **5**, 668–674.

Pierazzo E. and Artemieva N. (2012) Local and global environmental effects of impacts on Earth. *Elements* **8**, 55–60.

Roerdink D. L., Mason P. R. D., Farquhar J. and Reimer T. (2012) Multiple sulfur isotopes in Paleoarchean barites identify an important role for microbial sulfate reduction in the early marine environment. *Earth Planet. Sci. Lett.* **331–332**, 177–186.

Roerdink D. L., Mason P. R. D., Whitehouse M. J. and Reimer T. (2013) High-resolution quadruple sulfur isotope analyses of 3.2 Ga pyrite from the Barberton Greenstone Belt in South Africa reveal distinct environmental controls on sulfide isotopic arrays. *Geochim. Cosmochim. Acta* **117**, 203–215.

Sagan C. and Chyba C. (1997) The early faint sun paradox: organic shielding of ultraviolet-labile greenhouse gases. *Science* **276**, 1217–1221.

Savarino J., Romero A., Cole-Dai J., Bekki S. and Thiemens M. H. (2003) UV induced mass-independent sulfur isotope fractionation in stratospheric volcanic sulfate. *Geophys. Res. Lett.* **30**, 1–4.

Sforna M. C., van Zuilen M. A. and Philippot P. (2014) Structural characterization by Raman hyperspectral mapping of organic carbon in the 3.46 billion-year-old Apex chert, Western Australia. *Geochim. Cosmochim. Acta* **124**, 18–33.

Shen Y., Buick R. and Canfield D. E. (2001) Isotopic evidence for microbial sulphate reduction in the early Archaean era. *Nature* **410**, 77–81.

Shen Y., Farquhar J., Masterson A., Kaufman A. J. and Buick R. (2009) Evaluating the role of microbial sulfate reduction in the early Archean using quadrupole isotope systematics. *Earth Planet. Sci. Lett.* **279**, 383–391.

Toon O. B., Zahnle K., Morrison D., Turco R. P. and Covey C. (1997) Environmental perturbations caused by the impacts of asteroids and comets. *Rev. Geophys.* **35**, 41–78.

Ueno Y., Ono S., Rumble D. and Maruyama S. (2008) Quadrupole sulfur isotope analysis of ca. 3.5 Ga Dresser Formation: new evidence for microbial sulfate reduction in the early Archean. *Geochim. Cosmochim. Acta* **72**, 5675–5691.

Whitehill A. R. and Ono S. (2012) Excitation band dependence of sulfur isotope mass-independent fractionation during photochemistry of sulfur dioxide using broadband light sources. *Geochim. Cosmochim. Acta* **94**, 238–253.

Whitehill A. R., Xie C., Hu X., Xie D., Guo H. and Ono S. (2013) Vibrionic origin of sulfur mass-independent isotope effect in photoexcitation of SO_2 and the implications to the early earth's atmosphere. *Proc. Natl. Acad. Sci.* **110**, 17697–17702.

Whitehouse M. J. (2013) Multiple sulfur isotope determination by SIMS: evaluation of reference sulfides for $D^{33}S$ with observations and a case study on the determination of $D^{36}S$. *Geostand. Geoanal. Res.* **37**, 19–33.

Wolf E. T. and Toon O. B. (2012) Fractal organic hazes provided an ultraviolet shield for early Earth. *Science* **328**, 1266–1268.

Zerkle A. L., Claire M. W., Domagal-Goldman S. D., Farquhar J. and Poulton S. (2012) A bistable organic-rich atmosphere on the Neoarchean Earth. *Nat. Geosci.* **5**, 359–363.